Emergent Dipolar Order in Amphidynamic Crystals of a Metal Organic Framework with Polar Linkers Having Ultralow Rotational Barriers

Y.-S. Su[1,*], E. Lamb[1*], I. Liepuoniute[2], A. Chronister[1], P. Guzman[1], A. Stanton[1], S. Perez[2], T. Chang[2], K. N. Houk[2], M. Garcia-Garibay[2], and S. E. Brown[1]

[1]*Department of Physics & Astronomy, UCLA, Los Angeles, CA 90095, USA;*

[2]*Department of Chemistry and Biochemistry, University of California, Los Angeles, CA 90095, USA;*

Crystals built with a freely reorienting 2,2-difluoro-1,4-bicyclo[2.2.2]octane-dicarboxylate (F_2-BODCA) acting as linker and rotator in a paddle-wheel metal organic framework (MOF), with Zn(II)-nodes and 1,4-diaza-bicyclo[2.2.2]octane (dabco) spacers, revealed emergent order as a result of correlated dipole-dipole interactions. Spontaneous order was observed by variable temperature, frequency-dependent dielectric measurements consisting of a relatively sharp, frequency-independent change in capacitance at T_c = 100 K. This change occurred when a rapidly rotating, dipole-disordered, paraelectric phase, transformed into an ordered, antiferroelectric phase where dipole moments largely cancel each other. The dielectric response at lower temperature revealed a frequency-dependent Debye-like dynamic crossover as the rotor dynamics become slower than the frequency of the alternating electric field. The dynamic nature of the F_2-BODCA rotators was confirmed by low temperature NMR spectroscopy and the energetics of the rotational profile elucidated with the help of

*These authors contributed equally to this work.

Density Functional Theory (DFT) calculations, which also helped identify a thermally activated twisting of the F_2-BODCA as the motion that determines the dynamical crossover. Finally, Monte Carlo simulations on a 2D rotary lattice revealed a ground state with an Ising symmetry and reveal the effects of dipole-lattice and dipole-dipole interactions, strongly supporting expectations that freely rotating dipole lattices will display emergent behavior that arises from their intrinsic order and perturbations brought about by sufficiently strong external fields.

1 Introduction

Crystalline arrays of molecular rotors present unique opportunities to explore emergent phenomena [1]. As an example, it is expected that 1D, 2D and 3D arrays of molecular rotors bearing interacting electric dipoles will spontaneously order, where the broken symmetry depends on the relation between the rotational axis orientation and the underlying lattice symmetry [2], in a manner analogous to that displayed by the arrays of macroscopic compasses depicted in Fig. 1 [3,4]. For instance, 1D-dipole chains have a preferred ferroelectric alignment along the direction of the translation axis. Whereas, dipole orientation confined to a plane orthogonal to the translation axis leads to antiferroelectric ordering. Since the latter case constitutes a broken continuous symmetry, it is associated with a Goldstone mode: any orientation in the transverse plane is equally favorable. Similarly, the ground states of the ideal 2D and 3D arrays in Fig. 1 can adopt spontaneous ferroelectric or antiferroelectric order, and with one or more orientations that preserve the symmetry and energy of the assembly, enabling a range of applications associated with low energy

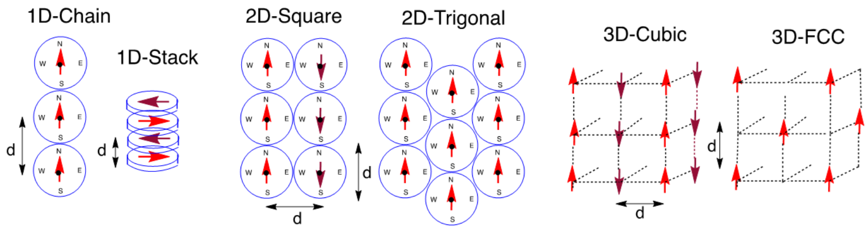

Figure 1: Broken symmetry states of classical rotary dipoles on lattices of different dimensionalities and symmetries.

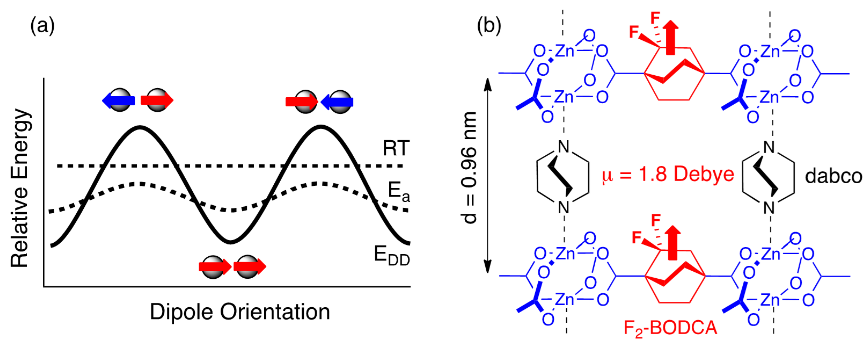

Figure 2: **a** Ideal conditions required for spontaneous dipolar order and correlated dipolar rotation represented for two dipoles in a chain. **b** Line structure of the metal organic framework MOF $Zn_2(F_2\text{-BODCA})_2(\text{dabco-}H_{12})$ with polar 2,2-difloro-bicyclo-[2.2.2]octane-1,4-dicarboxylate rotators.

long-wavelength excitations [5–7], or associated with the coupling to external fields [8–10], including electro-optic properties analogous to those of liquid crystals.

Classical order as depicted in Fig. 1 is generally expected when the thermal energy RT scale is of order the strength of the nearest-neighbor dipole-dipole interaction strength, E_{dd}. However, a state with considerable glassiness will result unless $E_{dd} \gtrsim E_a$, with E_a the variation in rotational potential associated with a dipole-lattice interaction and qualitatively illustrated in Fig. 2a.

From these three factors, the experimental challenge is the design of crystals with relatively low rotational barriers, which practically means that E_a is comparable to or ideally somewhat less than RT, with T corresponding to ambient temperature. If one specifically considers an ordering temperature of order 298 K or greater, one would need $E_a \lesssim 0.592$ kcal/mol, which implies rotational barriers on the same order of magnitude as the energy difference of a soft vibrational mode (*e.g.*, 207 cm^{-1} in this example). Fortunately, the solution to this challenge has been addressed systematically by us [11–13] and others [14–20], and a promising solution was recently found by taking advantage of metal organic frameworks (MOF) using a high symmetry bicyclo[2.2.2]octane rotator ($Zn_2(F_2$-BODCA$)_2$(dabco-H_{12})) [21], which was shown to have a barrier of only 0.2 kcal/mol (70 cm^{-1}). For this work, we selected the polar paddle wheel MOF $Zn_2(F_2$-BODCA$)_2$(dabco-H_{12}), consisting of layers of 2,2-difluoro-bicyclo[2.2.2.]octane-1,4-dicarboxylate (F_2-BODCA) rotators coordinated to dimeric zink(II) nodes with orthogonal 1,4-diazabicyclo[2.2.2.]octane (dabco) pillars that separate the layers. As described below, low-frequency dielectric and NMR spectroscopy measurements confirmed that the corresponding electric dipoles interact with the underlying lattice and with each other. At high temperature, the polar rotators are thermally disordered, and the dielectric response is Curie-Weiss-like, albeit with deviations close to T_c. A peak in the real part of the dielectric constant ϵ', observed at $T \simeq$100 K, is interpreted as evidence for a phase transition to an antiferroelectric state. The Curie-Weiss behavior is expected provided that the rotational potential is too large. This relationship is supported by Density Functional Theory calculations, which also provided the input for model Monte Carlo simulations performed on a square 2D rotary lattice.

2 Experimental results

2,2-Difluorobicyclo[2.2.2]octane-1,4-dicarboxylic acid (F_2-BODCA) was prepared by deoxofluorination of the diethyl 2-oxobicyclo[2.2.2]octane-1,4-dicarboxylate diester, as indicated in the Supplementary Information (SI). The reaction of F_2-BODCA with dabco and $Zn(NO_3)_2$•$6H_2O$ in dry dimethylformadide (DMF) at 120^{o}C afforded the pillared MOF Zn2(F_2-BODCA)$_2$(dabco). The as-synthesized material was activated at 200^{o}C for 2.5 h. Single crystals of Zn_2(F_2-BODCA)$_2$(dabco) were obtained after activation, and the diffraction study was made at 100 K. The crystal structure of Zn_2(F_2-BODCA)$_2$(dabco) was solved in the tetragonal space group P-4 with a weighted R-factor of 0.1114 (Fig. 3a). The structure consists of a 2D-squared grid formed by dicarboxylate ligands and zinc paddle wheel clusters ([Zn_2(F_2-BODCA)$_2$]), which coordinate to dabco in the orthogonal direction to complete the 3D structure (see also Figure S24). Additionally, the structure shows that both the dabco pillar and F_2-BODCA rotator are disordered. As the three-fold symmetric dabco spacers sit in a crystallographic center of symmetry, they occupy, on average, two positions related by a 60° rotation with equal probability. The F_2-BODCA rotator is positionally disordered with both sides of the structure occupied by the terminal F-atoms, also with equal probability. Although F_2-BODCA is in a general position, rotational disorder is manifested in the diffraction study by the distribution of the F atom electron density attached to several of the disordered carbon sites across the periphery of the F_2-BODCA cage.

Cross polarization and magic angle spinning (CP-MAS) ^{13}C NMR experiments confirmed the general features of the structure with a number of signals consistent with the time-average

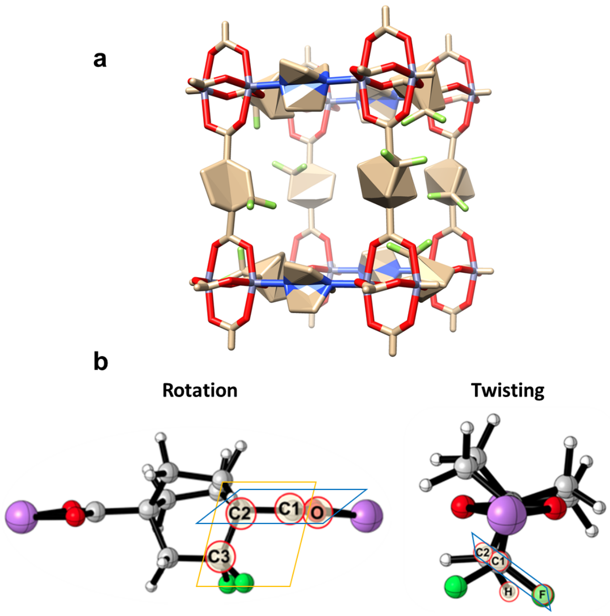

Figure 3: **a** Structure solution for the single crystal diffraction data of (F_2BODCA)-MOF at T=100 K, with a view near to the c-axis showing the positional and rotational disorder of the F_2BODCA rotors. **b** The M06-2X/6311+G(d,p) optimized structure of (F_2BODCA)-MOF. The rotation angle is between O-C1-C2 plane and C1-C2-C3 plane, whereas the twisting angle is between F-C1-C2 plane and C1-C2-H plane, respectively. The carboxylate groups (O-C-O) are coplanar and aligned along either the ac or bc crystal planes.

symmetry of the ligands, including two carboxylates and one carbon signal at low field that displays scalar coupling with the bound fluorine atoms for the rotator (see Figure S22). The activated material is thermally stable from room temperature to 300^{o}C, as demonstrated by thermal gravimetric analysis (TGA) (see Figure S26). The phase identity of the activated powder samples was confirmed by powder X-ray diffraction. The permanent porosity of Zn_2(F_2- BODCA)$_2$(dabco) was characterized by N_2 sorption at T=77 K, which followed a type I isotherm with a BET surface of 996 m^2 g^{-1} (see Figure S27).

The dielectric measurements were carried out on a powder sample using a 3-terminal capacitance setup configured for audio frequencies at 300 Hz, 1 kHz, and 10 kHz, for temperatures covering the range T =[20-270 K]. The resulting capacitance C and loss tangent $\tan\delta$ vs. temperature are shown in Fig. 4. The capacitance exhibits a cusp at $T \simeq 100$ K, with a weak decrease on further lowering temperature. This is followed by a sharp decrease below $35 - 45$K. A frequency-dependence is associated with the sharp decrease (and which is notably absent at higher temperatures). There is an accompanying loss peak in $\tan\delta$, which is also strongly frequency-dependent. Thus, the anomaly at T =100 K is interpreted as evidence for a phase transition, whereas the falloff in capacitance at lower temperatures is interpreted as a dynamical crossover.

Our goal is to extract some quantitative information from the dielectric response of the powder, which can then inform as to the rotator dynamics. From the crystal structure and ligand constraints, an anisotropic response is expected. With that caveat, we assume random grain orientation, and consider the angular average. Since the loss is relatively small at higher temperature

($T > 100$K), we take the capacitance as related to the plate geometry according to the elementary formula,

$$C_p = \frac{K_p \epsilon_0 A}{d} \tag{1}$$

where ϵ_0 is the permittivity of vacuum, K_p is the effective dielectric response of the powder, and A, d are area cross-section and distance between the plates, respectively. The packing density of the grains is less than 100%; our estimate, based on geometry and mass considerations is $\sim 65-70\%$. To account for the incomplete volume fraction α, we apply Böttcher's formula [22],

$$\frac{K_p - 1}{3K_p} = \frac{\alpha(K_s - 1)}{K_s + 2K_p} \tag{2}$$

where K_s is the response for the sample. In isolating the response associated with the dipolar rotator degrees of freedom (χ_r) from what is expected to be a temperature- and frequency-independent background (χ_b), we rewrite the total as the sum of two distinct contributions, $K_s = 1 + \chi_r + \chi_b$. The rotator response χ_r is considerecd to follow a Curie-Weiss form at high temperature,

$$\chi_r = \frac{np^2}{2k_B\epsilon_0(T + \Theta)}, \tag{3}$$

with n the number of rotator per unit volume in the crystalline structure, Θ the Curie temperature, k_B Boltzmann constant, ϵ_0 vacuum permittivity, and p is the effective electric dipole moment of the rotator. The factor 2 in the denominator is a geometric factor associated with the single-axis rotation. Following the subtraction of an inferred background, $\chi_r = K_s - (1 + \chi_b)$, with $(1 + \chi_b) \simeq 4.4$, $1/\chi_r$ *vs.* T is shown in the inset of Fig. 4a. Taking the high-temperature portion to be linear and using $\alpha = 0.7$, p=2.2 Debye is obtained. There is an approximate agreement with the calculated result, 1.8 Debye, previously obtained from the AM1 method using Spartan software

[23], and is close to that derived from hybrid functional M06-2X/6-311+G(d,p) quantum mechanical method using Gaussian[24]. The characteristic temperature, as shown in the inset of Fig. 4a, is Θ = +150 K.

As a means for parameterizing the dynamical crossover, Debye-like relaxation is assumed. Therefore, the real part K' and loss $tan\delta$ are expressed as:

$$K' = 1 + \chi_b + \frac{\chi_r(0)}{1 + (2\pi f\tau)^2}, \tag{4}$$

$$\tan\delta = \frac{\chi_r(0)(2\pi f\tau)}{[1 + \chi_r(0) + \chi_b] + [(1 + \chi_b)(1 + (2\pi f\tau)^2)]}. \tag{5}$$

where $1 + \chi_b \simeq$ 4.4 and $\chi_r(0)$=1.6 correspond to the real-part high and low frequency extrapolations, respectively, and $2\pi f$ is the angular frequency of the applied electric field. The characteristic relaxation time τ is taken to follow a simple thermally activated behavior as:

$$\tau = \tau_0 \exp(\frac{\Delta}{k_B T}), \tag{6}$$

where Δ is an activation barrier for rotation. Loss peaks are determined by the condition $2\pi f\tau = 1$; where it is satisfied is depicted in Fig. 5, with measurement frequency serving as an implicit parameter. The three lines are the expected variation for an activated relaxation process; the bold (green) line corresponds to $\tau_0 = 3.4 \times 10^{-10} s$, Δ=1.2 kcal/mol. As described below, complementary experimental information on rotator dynamics from ^{19}F NMR are consistent with a common relaxation process.

The temperature dependence over the range $T = 35 - 120K$ of the ^{19}F spectral Full Width at Half Maximum (FWHM), ($^{19}\delta\nu$) in Fig. 6 reveals that the broadening occurs in two steps upon

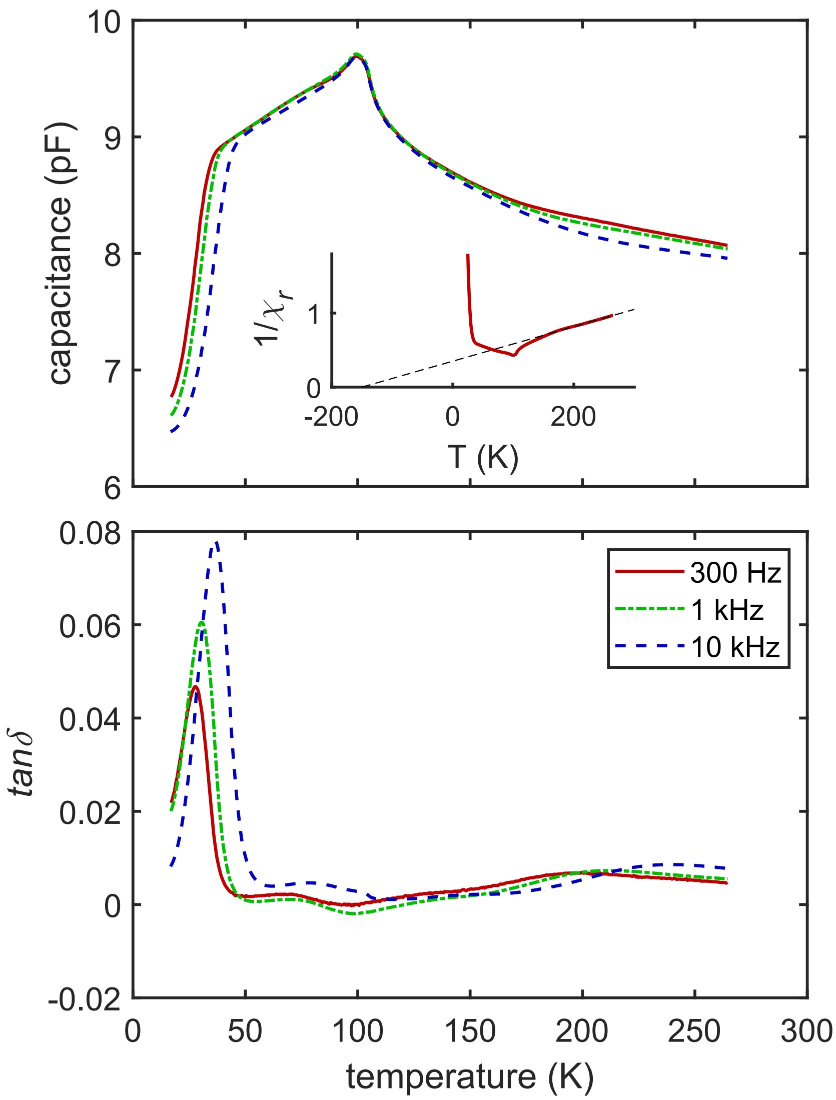

Figure 4: (a) Capacitance vs. temperature T, at reference frequencies f=300 Hz, 1 kHz, 10 kHz. *Inset:* Curie-Weiss analysis is consistent with overall antiferroelectric coupling, with an inferred background $1 + \chi_b \simeq 4.4$, Θ= +150 K (b) $tan\delta$ vs. T, measured at the same frequencies as capacitance. The most prominent feature is a substantial loss peak, which for each frequency measured is observed to occur at the crossover temperature in the real capacitance. The behavior is indicative of a dynamical freezeout, which is interpreted in the framework of Debye-like relaxation.

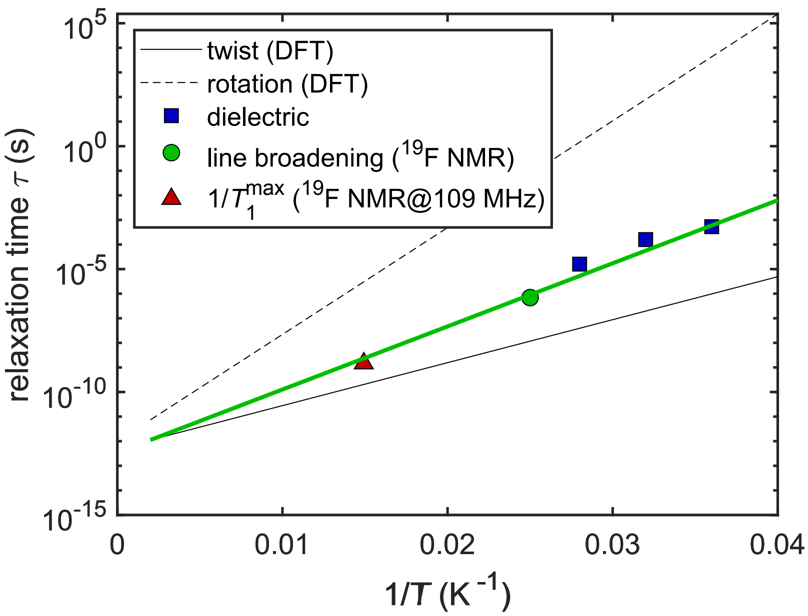

Figure 5: Comparison of the time scales from DFT calculations, NMR linewidth and relaxation rate, and dielectric measurements. The solid black positively sloped line is based on DFT twisting motion (0.8 kcal/mole potential depth). The bold green line is plotted with the activation energy for the DFT twist multiplied by a factor of 1.5.

cooling. The measurements were carried out at a field strength of B_0=2.72T and carrier frequency 109.83 MHz. At temperatures $T \gtrsim$105 K, the observed FWHM is ~ 13 kHz. As the temperature is reduced below 105 K, the FWHM is observed to increase before leveling off below about 90 K. Another onset of line broadening sets in on cooling below approximately T=40 K, below which $^{19}\delta\nu = 27.50$ kHz. We associate the two increases in linewidth with the phase transition, and the dynamical crossover. In the second case, the broadening is expected as the characteristic time scale slows down to be of order of the observed linewidth. Thus, the solid green circle in Fig. 5 corresponds to $^{19}\delta\nu = 27.50$ kHz, and $T = 40$ K. Additional dynamical information was gleaned from a peak in the spin-lattice relaxation rate, modeled using the standard Bloembergen-Pound-Purcell (BPP) analysis. The associated characteristic relaxation time is also included in Fig. 5.

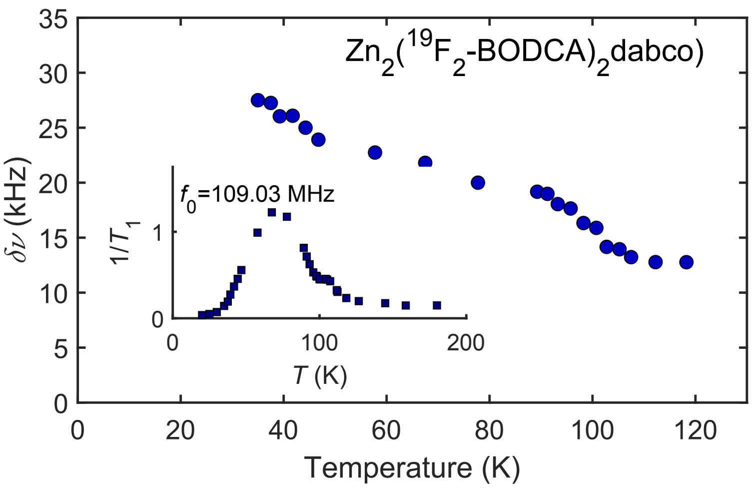

Figure 6: Temperature dependence of NMR linewidth FWHM $^{19}\delta\nu(T)$. Increases are observed in two independent temperature ranges, $T \lesssim 100$ K, and $T \lesssim 40$ K, which are attributed to phase transition and freezing of the rotators respectively. Line broadening is expected to occur at a crossover where time scale of the dynamics is of the order of $\delta\nu$. The inset is the ^{19}F NMR spin-lattice relaxation time as a function of temperature at the same magnetic field.

3 Density Functional Theory Calculations

In order to identify the energy barrier corresponding to the activated relaxation, and otherwise to guide the analysis of the rotor interactions and dynamics, we carried out DFT [24] calculations of (F_2BODCA)-MOF motion. Our calculations were executed on an isolated molecule containing the F_2BCO group linked to assumed lithium atoms to avoid repulsive interactions between the carboxylate ions and the electronegative fluorine atoms. To mimic the crystal lattice environment, the two carboxylate groups were constrained to be co-planar, namely in the ac plane or bc plane as indicated in Figs. 2,7. The calculations were carried out using the M06-2X/6–311+G(d,p) hybrid functional method [25]. Starting from the optimized structure, potential energy surface calculations were performed by scanning rotational and enantiomeric twisting dihedral angles, as illustrated in Fig. 3. The rotational angle was defined as the one between the plane of the carboxylate groups (O-C1-C2) and plane constructed by (C1-C2-C3), whereas the twisting angle was between (C1-C2-H) and (C2-C1-F) planes. Twisting reduces the D_3h symmetry to D_3 symmetry and overall, the oscillations explore the twisted D_3^+ and D_3^- structures as indicated in Fig. 7. The energy minima are found to be in the twisted conformation (D_3^+ or D_3^-) with fluorine atoms positioned away from the plane of the carboxylate groups, namely pointing in the ab plane.

Frequency calculations for the ground state structure yielded one imaginary frequency corresponding to the partial rotation of one of the carboxylate groups. This imaginary frequency arises due to the in-plane constraint. As expected, the transition state (TS) conformation was found with one imaginary frequency. The structure has a close approach to an oxygen of a carboxylate and the fluorine ions of F_2BCO. The imaginary frequency corresponds to the twisting and rotation of F_2BCO, and the transition state involves the coupled motion of the system. The DFT calculated barriers for independent enantiomeric twisting and rotation are 0.8 kcal/mol and 2.0 kcal/mol, respectively, with uncertainty in the range of 0.2 to 0.4 kcal/mole [21]. The barrier for the coupled rotation-twist is calculated to be 1.4 kcal/mol. For the unsubstituted BCO rotator [21], the two-fold symmetry of the stationary carboxylate groups and the three-fold symmetry of the rotator combine to give a six-fold symmetric rotator. The functionalized BODCA system breaks the symmetry and its associated coupled motion yields a potential with a point of interconversion between the two two-fold wells associated for each D_3^+ and D_3^- conformer. The lowest energy trajectory connects the two minima diagonal to each other and explores the D_3^+, D_3h, and D_3^- structures as shown in Fig. 8a. While the two fold rotational potential accounts for the two orientations that determine the dynamics of order-disorder transition, dipole oscillations above and below the ab-plane enabled by the twisting process are proposed to account for the dielectric behavior and Debye freezing in the ordered phase. The temperature dependence of this process (0.8 kcal/mol) is indicated in Fig. 5 by the thin black line, with a slope that is reasonably close to the experimental one indicated by the green line.

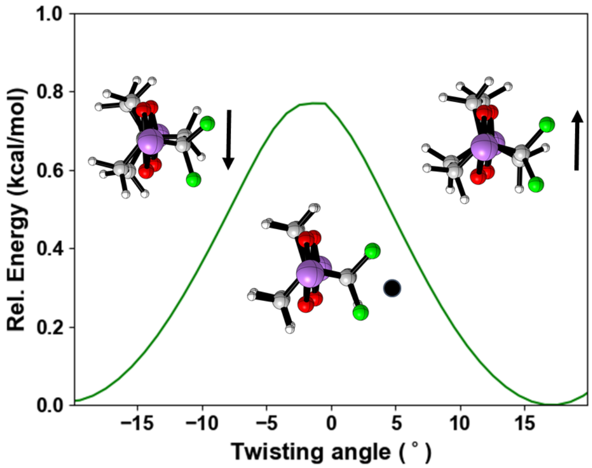

Figure 7: DFT energy scan of enantiomeric twisting as calculated using M06-2X/6-311+G(d,p) quantum mechanical method. The twist angle ranges from -20^o to +20^o, which would modulate the orientation and magnitude of the component of the dipole moment along the c-axis. The calculated potential energy barrier is 0.8 kcal/mol with a twisting attempt-to-escape frequency of 65.80 cm^{-1} ($1.97 \times 10^{12} s^{-1}$). These values indicate a twisting frequency of c.a. 10 kHz at 20 K, which is reasonably close to the temperature regime where the dielectric freeze-out behavior occurs. It is worthwhile to note that the 0.8 kcal/mol corresponds well to the activated behavior as simulated with the combined data of dielectric Debye-like freezeout and NMR linewidth shown in Fig. 5.

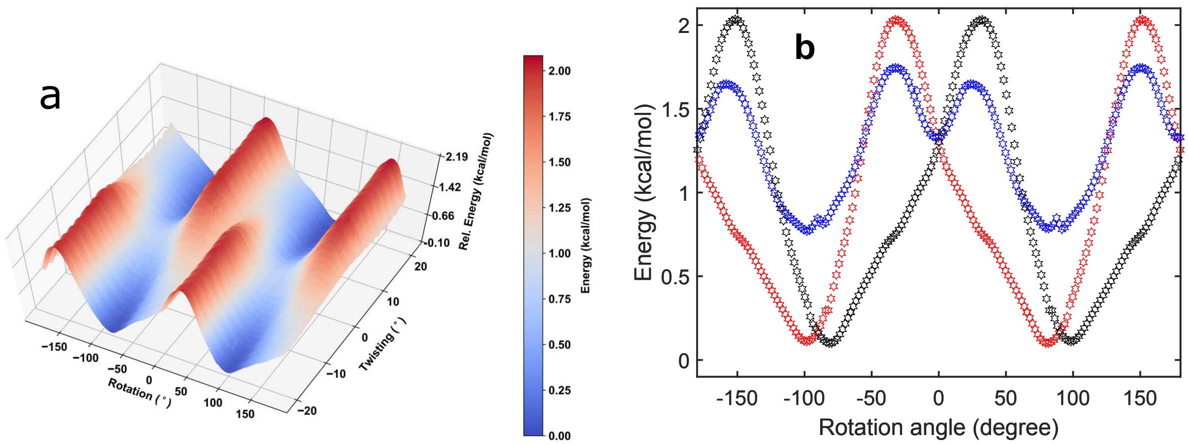

Figure 8: **a** DFT lattice potential energy landscape. The x- and y-axes indicate the rotational and enantiomeric twisting angles. **b** Cuts of the above DFT energy landscape at twist angle c.a. +20^o,-20^o (red and black), 0^o(blue) of the F_2BCO. The rotational angle ranges from -180^o to 180^o, and the calculated independent rotational energy barrier is $\sim$2.0 kcal/mol for -20^o and -20^o twist. The ground state conformation has fluorine atoms pointing away from the carboxylate oxygens. In particular, it is worthwhile to note that the coupling of the twisting and rotational degrees of freedom amounts to $\sim$1.4 kcal/mole lattice potential, which is lower than that of independent rotation. Technical details of calculation can be found in the Supplementary Information.

4 Monte Carlo Simulations

The consequences on the parelectric-antiferroelectric phase transition of a similar, or greater energy scale for the rotor-lattice rotational potential, when compared to the near-neighbor electric dipole interactions, were explored using a classical Monte Carlo simulation. For simplicity, our model assumed uniform, point dipole moments arranged in a lattice of alternating a/b rotation axes. The cases of nearest-neighbor (NN) only, and NN plus next-nearest-neighbor (NNN) electric dipole-dipole interactions. The rotational potential energy associated with rotor-lattice interaction was varied as well. see Fig. 9. The dipole moment for a single rotator was taken to be 1.8 Debye in the simulation. The MOF structure constrains the dipole polarization vector to rotations about the ligand bonding axis. If near-neighbor dipole-dipole interactions dominate, then the simulated ground state exhibits an ordered phase with dipole moments all lying in the ab plane, such that the underlying universality class is Ising. The ground state is shown in Fig. 9.

The sublattice polarization is shown as a function of temperature for various lattice potential amplitudes in Fig. 10. The general trend is a modestly increasing ordering temperature for the reduced thermally activated rotations resulting from increased lattice potential amplitudes. The overall normalization for the temperature corresponds to

$$k_B T_0 = \frac{p^2}{4\pi\epsilon_0 \langle d^3 \rangle}, \tag{7}$$

where k_B is Boltzmann constant, p is the rotor ligand dipole moment, ϵ_0 is vacuum permittivity, and d is the NN separation. For the range of strengths of relative lattice potential studied, quenched disorder does not significantly diminish the observed degree of ordering.

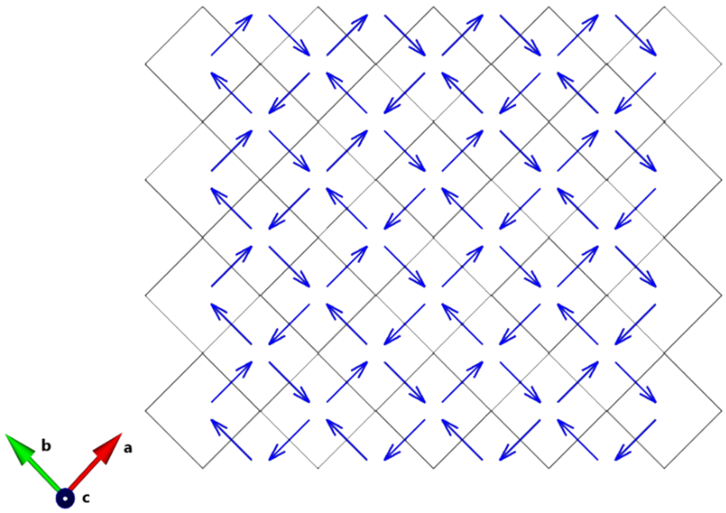

Figure 9: The simulated ground state of the spatial electric dipole configuration below the 100K phase transition. The electric dipole moments all lie in the ab plane with alternating directions. If we decompose the dipole moments into two orthogonal components, they respectively form antiferroelectric configurations. The interaction under consideration are the electric dipole-dipole coupling among the first nearest neighbors and the second nearest neighbors. Each electric dipole moment is considered as 1.8 Debye.

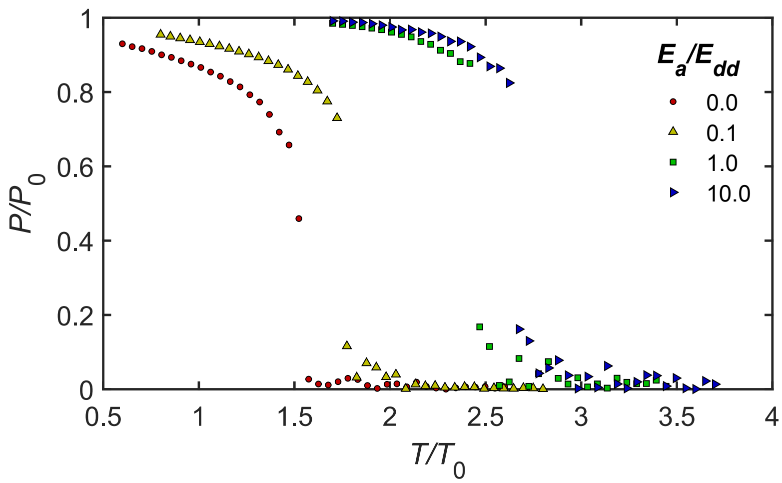

Figure 10: Temperature dependence of polarization of a sublattice given by Monte Carlo simulation, where the form of lattice potential input was assumed to be sinusoidal with 2-fold symmetry. Dipolar interaction and lattice potential with varied values as normalized to nearest-neighbor dipole-dipole interaction are taken into account.

5 Conclusion

Crystalline molecular rotors are a promising system for collective molecular machines since its correlated motion of the rotating molecules plays a pivotal role in realizing controllable machines responsive to external stimuli. The functionalized material system studied here, $Zn_2(F_2$-BODCA$)_2$(dabco-H_{12}) molecular rotors, were fabricated and characterized by powder X-ray diffraction revealing its tetragonal lattice with alternating layers of polar rotors on the a-b plane and nonpolar rotors with axis parallel to c direction. Variable-temperature dielectric measurements unveiled two features, one corresponding to a phase transition at $T_c = 100$ K, and a second is associated with a dynamical crossover occurring at lower temperatures. The observed transition temperature corresponds well to the expected nearest neighbor dipole-dipole coupling strength. Monte Carlo simulations including nearest neighbor and next nearest neighbor couplings reveal an antiferroelectric ordering, also in the appropriate temperature range.

DFT calculation provided the conceptual framework in relation to the observed dynamical crossover. Namely, the lattice potential stiffness is controlled by a thermally activated internal twisting of the rotors. As the twisting is frozen out, the effective rotational motion is suppressed, with the affect of suppressing the dielectric response.

The results of our study indicate that the rotational potential energy barrier is sufficiently small that the dipole-dipole interaction drives an antiferroelectric phase transition. Our work suggests that fluorine-grafted crystalline molecular rotors bearing correlated behaviors is an auspicious material platform to be utilized as a responsive machine component on the nanoscale in the foreseeable future.

Supplementary information. This section includes synthetic procedures, analytical data and spectroscopic characterization of all the precursors needed for the preparation of $Zn_2(F_2$-BODCA$)_2$(dabco) and supporting analytical, diffraction and NMR characterization data with the crystalline material.

1. Kottas, G. S., Clarke, L. I., Horinek, D. & Michl, J. Artificial molecular rotors. Chem. Rev. **105**, 1281–1376 (2005).
2. Rozenbaum, V. M. Long-range orientational order in a two-dimensional degenerate system of dipoles on a square lattice. JETP Lett. **63**, 662–667 (1996).
3. Adams, D. Calculating the low temperature vapour line by monte carlo. Molecular Physics **32**, 647–657 (1976).
4. Vogelsberg, C. S. & Garcia-Garibay, M. A. Crystalline molecular machines: function, phase order, dimensionality, and composition. Chem. Soc. Rev. **41**, 1892–1910 (2012).
5. DeLeeuw, S. W., Solvaeson, D., Ratner, M. A. & Michl, J. Molecular dipole chains: Excitations and dissipation. J. Phys. Chem. B **102**, 3876–3885 (1998).
6. Sim, E., Ratner, M. A. & de Leeuw, S. W. Molecular dipole chains ii. J. Phys. Chem. B **103**, 8663–8670 (1999).

7. de Jonge, J. J., Ratner, M. A., de Leeuw, S. W. & Simonis, R. O. Molecular dipole chains iii: Energy transfer. J. Phys. Chem. B **108**, 2666–2675 (2004).

8. Vacek, J. & Michl, J. Molecular dynamics of a grid-mounted molecular dipolar rotor in a rotating electric field. Proc. Natl. Acad. Sci. U.S.A. **98**, 5481–5486 (2001).

9. Vacek, J. & Michl, J. Artificial surface-mounted molecular rotors: Molecular dynamics simulations. Adv. Funct. Mater. **17**, 730–739 (2007).

10. Neumann, J., Gottschalk, K. E. & Astumian, R. D. Driving and controlling molecular surface rotors with a terahertz electric field. ACS Nano **6**, 5242–5248 (2012).

11. Garcia-Garibay, M. A. Crystalline molecular machines: Encoding supramolecular dynamics into molecular structure. Proc. Natl. Acad. Sci. U.S.A. **102**, 10771–10776 (2005).

12. Khuong, T.-A. V., Nuñez, J. E., Godinez, C. E. & Garcia-Garibay, M. A. Crystalline molecular machines: A quest toward solid-state dynamics and function. Acc. Chem. Res. **39**, 413–422 (2006).

13. Howe, M. E. & Garcia-Garibay, M. A. The roles of intrinsic barriers and crystal fluidity in determining the dynamics of crystalline molecular rotors and molecular machines. J. Org. Chem. (2019).

14. Shima, T., Hampel, F. & Gladysz, J. A. Molecular gyroscopes: $[fe(co)_3]$ and $[fe(co)_2(no)]^+$ rotators encased in three-spoke stators; facile assembly by alkene metatheses. Angew. Chem. Int. Ed. **43**, 5537–5540 (2004).

15. Akutagawa, T. et al. Ferroelectricity and polarity control in solid-state flip-flop supramolecular rotators. Nat. Mater. **8**, 342–347 (2009).

16. Setaka, W. & Yamaguchi, K. A molecular balloon: Expansion of a molecular gyrotop cage due to rotation of the phenylene rotor. J. Am. Chem. Soc. **134**, 12458–12461 (2012).

17. Setaka, W. & Yamaguchi, K. Order-disorder transition of dipolar rotor in a crystalline molecular gyrotop and its optical change. J. Am. Chem. Soc. **135**, 14560–14563 (2013).

18. Comotti, A. et al. Engineering switchable rotors in molecular crystals with open porosity. J. Am. Chem. Soc. **136**, 618–621 (2014).

19. Yao, Z.-S., Yamamoto, K., Cai, H.-L., Takahashi, K. & Sato, O. Above room temperature organic ferroelectrics: Diprotonated 1,4-diazabicyclo[2.2.2]octane shifts between two 2-chlorobenzoates. J. Am. Chem. Soc. **138**, 12005–12008 (2016).

20. Bracco, S. et al. Ultrafast molecular rotors and their co_2 tuning in mofs with rod-like ligands. Chemistry - A European Journal **23**, 11210–11215 (2017).

21. Vogelsberg, C. S. et al. Ultrafast rotation in an amphidynamic crystalline metal organic framework. Proc. Natl. Acad. Sci. U.S.A. **114**, 13613–13618 (2017).

22. Böttcher, C. J. F. Theory of Electric Polarization, vol. 1 (Elsevier, 1973), 2 edn.

23. Dominguez, Z. et al. Molecular compasses and gyroscopes with polar rotors: Synthesis and characterization of crystalline forms. J. Am. Chem. Soc. **125**, 8827–8837 (2003).

24. Frisch, M. e. a. Gaussian09. Tech. Rep., Gaussian, Inc., Wallingford, CT (2013).

25. Zhao, Y. & Truhlar, D. G. The m06 suite of density functionals for main group thermochemistry, thermochemical kinetics, noncovalent interactions, excited states, and transition elements: two new functionals and systematic testing of four m06-class functionals and 12 other functionals. Theor. Chem. Acc. **120**, 215–241 (2007).

Acknowledgements This work was supported in part by the National Science Foundation under grants DMR-1709304, DMR-1700471 and MRI-1532232 (solid state NMR).

Author Contributions S. P. and M. G.-G. conceived of the material synthesis, M. A. G.-G., S. P., and S. E. B. conceived of the experiments, E. L. designed, constructed, and tested the dielectric apparatus, Y.-S. S. and E. L. performed the dielectric and cryogenic NMR measurements, E. L. and A. S. wrote and executed the Monte Carlo Simulation, I. L. performed the DFT calculations. Y.-S. S., S. E. B., and M. A. G.-G. wrote the manuscript with contributions from all the other authors.

Competing Interests The authors declare that they have no competing financial interests.

Correspondence Correspondence and requests for materials should be addressed to Y.-S. Su (yssu@physics.ucla.edu), I. Liepuoniute (ieva@.ucla.edu), M. A. Garcia-Garibay (mgg@chem.ucla.edu), or S. Brown (brown@physic.ucla.edu)